Chemical Engineering Science 309 (2025) 121465

Contents lists available at ScienceDirect

Chemical Engineering Science

journal homepage: www.elsevier.com/locate/ces

Fluid distribution in artificially manufactured porous mixed-wetting materials as a model for gas diffusion electrodes

Sebastian Brosch [a,1], Thorben Mager [b,1,*], John Linkhorst [c], Ulrich Nieken [b], Matthias Wessling [a,d,*]

[a] Chemical Process Engineering, RWTH Aachen University, Forckenbeckstr. 51, Aachen, 52074, NRW, Germany
[b] Institute for Chemical Process Engineering, University of Stuttgart, Böblinger Str. 78, Stuttgart, 70199, BW, Germany
[c] Process Engineering of Electrochemical Systems, Technical University Darmstadt, Otto-Berndt-Str. 78, Darmstadt, 64287, HE, Germany
[d] DWI - Leibniz Institute for Interactive Materials, Forckenbeckstr. 50, Aachen, 52074, NRW, Germany

ARTICLE INFO

Keywords:
Micromodel
Smoothed particle hydrodynamics
Multiphase flow in mixed wetting porous media
Microfluidics
Heterogeneous wetting

ABSTRACT

Mixed wettability of porous media plays a crucial role in processes involving enhanced oil recovery, catalysis, membrane filtration and porous electrodes. To comprehend, optimize and implement these processes, a comprehensive understanding of the influence of spatial surface energy distribution on wettability is pivotal. Direct measurement of fluid distributions in porous media is challenging. Therefore, direct numerical simulation (DNS) is often employed. We propose a microfluidic device incorporating hydrophilic and hydrophobic surfaces with wetting properties comparable to silver-based gas diffusion electrodes. Displacement experiments were conducted to validate simulation predictions. Experimental findings were compared to Smoothed Particle Hydrodynamics (SPH) simulations. We observed the following key details: (a) Our micromodel accurately depicts mixed wettability. (b) Implementation of a 2D + 1D simulation captures real wetting phenomena. (c) Comparisons between experiment and simulation reveal the impact of cornerflow. This coupled approach facilitates planned design of porous media and fosters the understanding of transport in microporous networks.

1. Introduction

Mixed-wetting of porous media plays an important role in different processes. Among these are enhanced oil recovery, heterogeneous catalysis, membrane filtration, surface coatings or drug delivery systems (Xu et al., 2020; Mousavi et al., 2024; Agbalaka et al., 2008; Anderson, 1987; Błaszczyk et al., 2024). Particularly in the design of porous catalysts, mixed wettability is applied in reactions involving liquid/solid/gas phase boundaries and was shown to increase selectivity and efficiency of the reaction (Xu et al., 2020). Through the electrification of industry, an additional field of application for porous catalysts became relevant. Gas diffusion electrodes (GDEs) are applied in electrolysis processes like CO_2 (Burdyny and Smith, 2019) or HCl reduction (Bechtel et al., 2021) and the industrially relevant chlor-alkali electrolysis (Moussallem et al., 2008) with an energy demand of at least 195.8 TW h in 2017 (Kintrup et al., 2017).

The GDE is exposed to an electrolyte on one side and a gas phase on the opposite side to establish intense contact between the electrolyte and gas. Similar configurations are found in oil recovery or surface coatings, where a high contact between the different phases enhances the efficiency of the process. *In situ* analysis of fluid distribution is often challenging. In the field of oil recovery, multiple different methods and model systems were presented in the past years. Different techniques for fluid visualization can be employed: microvisualization relies on injecting porous media with resins, that harden in place and represent the phase distribution *post mortem* (Yadav et al., 1987). More recently, X-ray micro tomography was used to investigate wettability in situ (Alhammadi et al., 2017). Beyond that, mainly, simulations are used to obtain information on fluid distribution in mixed-wetting porous media (Zhao et al., 2010; Agbalaka et al., 2008). In other fields, mixed wettability can be measured more easily. In surface coatings in particular, the effect of different contact angles on wettability is a readily accessible metric. As one example for applicaiton, superhydrophilic and superhydrophobic can be combined to prevent ice formation on airplane wings (Mousavi et al., 2024). In GDEs, a non-wetting material like polytetrafluoroethylene (PTFE) is added to prevent the liquid electrolyte from fully penetrating the electrode. As shown by Franzen et al. (2019), the amount and local distribution of PTFE strongly influence the electrochemical performance of the electrodes due to changes in the electrolyte distribution inside the GDE. While the porous structure, as well as the

* Corresponding authors.
E-mail addresses: thorben.mager@icvt.uni-stuttgart.de (T. Mager), manuscripts.cvt@avt.rwth-aachen.de (M. Wessling).
[1] These authors contributed equally to this work.

https://doi.org/10.1016/j.ces.2025.121465
Received 4 November 2024; Received in revised form 25 February 2025; Accepted 28 February 2025
Available online 2 March 2025

distribution of PTFE inside the GDE, can be spatially resolved (e.g. by FIB-SEM techniques, see Franzen et al. (2019)), the local distribution of electrolyte in the membrane can not be determined with high resolution today. Methods applied to determine electrolyte distribution in gas diffusion layers (Niblett et al., 2023; Paulisch et al., 2021) cannot be applied to microporous electrodes due to the high adsorption of radiation by the metal. Thus, Direct Numerical Simulation (DNS) of the electrolyte imbibition in the mixed-wet porous structure is currently the best approach to obtain electrolyte distributions in GDEs. DNS relies on a validated model that accounts for the local wetting properties of the pore wall, which can be either a wetting (metal) or a non-wetting material (such as PTFE).

Overall, it is clear that mixed wettability is an important phenomenon that needs to be understood to enable optimal implementation of several processes. In particular, emerging electrochemical technologies incorporating GDEs are sensible to changes in wettability due to their complex porous structure incorporating different materials.

To validate our DNS simulations, an optically accessible microfluidic channel incorporating both wetting and non-wetting pillars was fabricated and experiments were conducted showing the displacement of a wetting phase (water) by a non-wetting phase (perfluorinated solvent Fluorinert FC-770). Microfluidics offers a high degree of control over the geometry, phase composition, and process conditions, while all processes within the model electrode can easily be observed using optical or fluorescence microscopy (Kalde et al., 2022a,b; Brosch et al., 2024). Coupling experimental observations with simulations of the same process offers significant insights into the underlying phenomena and enables validation of the computational model (Maier et al., 2024). Using algorithms based on contact angles of differently wetting surfaces, with little computational expense it is possible to obtain good estimates of water intrusion into reconstructed porous networks. However, these algorithms calculate electrolyte distribution based on weighted contact angles of a pore network and do not take typical fluid dynamics (mass or momentum balance) into account (Wiesner et al., 2024). The Smoothed Particle Hydrodynamics (SPH) method is used here for Direct Numerical Simulation as a powerful tool to model the moving interfaces. With SPH, surface tension, moving contact lines, and the resulting wetting phenomena can be described from first principles (Monaghan, 1992; Gingold, 1977; Shadloo et al., 2016).

Bandara et al. (2013) used SPH to reproduce the displacement experiments published by Lenormand et al. (1988) and Zhang et al. (2011). Here, wetting was modeled by the pair-wise-force model, originally introduced in SPH by Tartakovsky and Meakin (2005). An additional artificial force between fluid and wall particles was introduced to model the wetting behavior. Different capillary numbers and viscosity ratios, as well as the influence of the pore heterogeneity, were investigated over a large range of capillary or viscous fingering and stable displacement regimes. While qualitatively, all regimes were reproduced, differences in the flow paths were observed due to local heterogeneity and three-dimensional effects that were not introduced in their numerical model. Patino-Narino et al. showed the applicability of SPH to predict the three-phase flow behavior in a cross-like microfluidic device (Patino-Narino et al., 2019). They observed a very similar surface evolution compared to experiments using the surface tension formulation proposed by Hu and Adams (2006). Huber et al. (2016) introduced a volumetric reformulation of the unbalanced Young force to calculate dynamic contact angles. This Contact-Line-Force (CLF) model was later used by Kunz et al. (2019) to model flow in microfluidic channels. They simulated quasi-static and dynamic drainage experiments and compared them to a micromodel for a uniformly wettable structure. While saturation and non-wetting-phase distribution were in good agreement, the main differences were observed for the dynamics of the drainage. Recently, Mohammadi et al. (2024) used the SPH method to investigate the influence of flow rate, contact angle, and heterogeneity on the imbibition and drainage dynamics of a randomly generated porous media with smooth and rough surfaces and validated their model against analytical test cases. However, they assumed a homogeneous medium without varying local wetting behavior and did not show a comparison to experimental results.

In this study, we expand on previous efforts by validating a SPH model by simulation of a mixed-wetting material. To achieve this, we manufacture an artificially designed structure with heterogeneous wettability. To attain adjustable, yet comparable wetting properties, we replace the solid wall materials, as well as the wetting and non-wetting fluids, with novel materials specifically chosen to adjust the wetting properties within the domain. In this publication, the outline is as follows: First, we introduce the experimental setup and the fabrication of the microfluidic chip. Next, we explain the measurement of physical properties, especially the measurement of the contact angle as the most important physical property. The experimental control of the wetting is ensured by manipulating the pressure difference across the microfluidic device. Then, we describe our physical model and details of the numerical methods. To ensure correct calculation, we validate our SPH model against an analytical model for a mixed-wet single-pore. Next, the same pore was investigated experimentally. This experimental setup allows for a direct comparison between the experimental results and simulation results. Finally, we conduct a comparative analysis of the filling process of an artificial mixed-wetting channel consisting of multiple pores of different sizes and surface properties. We discuss the results of displacement experiments and their comparison with simulated predictions.

2. Experimental methods

2.1. Single-pore model

Heterogenous wetting was established with two geometrical different types of Hele-Shaw-Cells. Both were designed using Autodesk Inventor 2023. The first one is the most basic system, a single pore with one hydrophilic and one hydrophobic side to a constriction. The heterogeneous wettability is established by the combination of a hydrophilic acrylate-based polymer and hydrophobic PDMS.

The overall dimensions of all channels were chosen so that manufacture of the channels and imaging of wetting within was possible under ideal conditions and to ensure that the Hele-Shaw condition is fulfilled. The Hele-Shaw condition states that $Re\left(\frac{H_{\text{app}}}{W_{\text{app}}}\right) = \frac{\rho|v|H_{\text{app}}^2}{\mu W_{\text{app}}} \ll 1$, which is given for our geometry. Manufacture of the hydrophilic regions as well as imaging of the phase boundary give optimal results at channel heights at or below 100 µm.

Fig. 1 shows the geometrical setup. Two pillars, each with a radius of $R_p = 400\,\mu\text{m}$ were placed opposite each other in a straight channel with channel width $W_{app} = 200\,\mu\text{m}$. The pillar centers were placed such that the narrowest constriction of the converging-diverging geometry has a width of $W_i = 100\,\mu\text{m}$. Thus, the pillar centers have a distance of

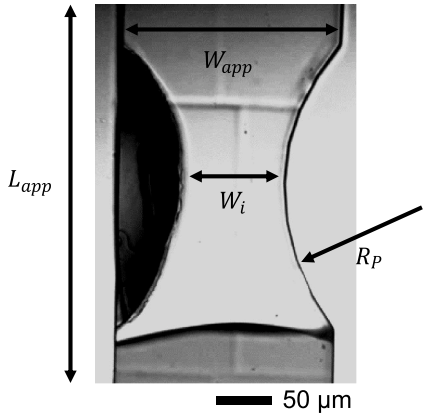

Fig. 1. Geometrical parameters of the single pore system.

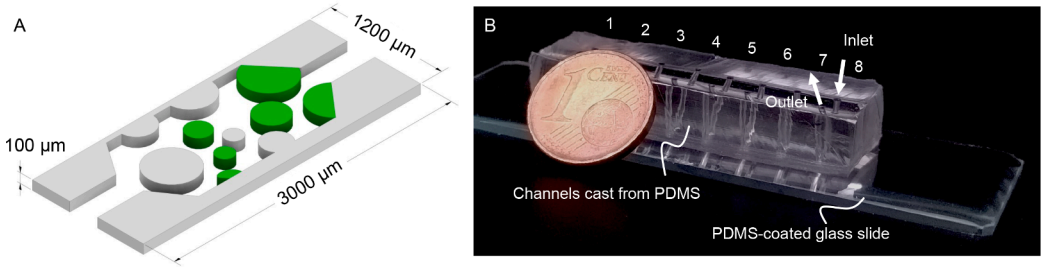

Fig. 2. Fabricated microfluidic chip for experimental observation. A: CAD Model of the microfluidic model GDE comprising of outer walls and pillars with different surface properties. The hydrophobic phase is shown in gray, and the hydrophilic one in green. B: Photo of the assembled microfluidic chip. For parallelization of production, eight model GDEs are produced at a time on a single chip.

$W_p = 2 \cdot R_p + W_i = 500\,\mu m$. The length of the channel considered was $L_{app} = 600\,\mu m$. The channel height in the third dimension is constant at $H_{app} = 90\,\mu m$. The hydrophilic pillar was created by printing an acrylate pillar into the channel, as described in Section 2.3. By changing the pressure difference between the inlet and outlet, the water-Fluorinert phase boundary is moved through the pore. Saturation and phase boundaries can be determined for each pressure step.

2.2. Full-pore model

To investigate mixed wetting behavior in porous media with multiple pores, a second Hele-Shaw-Cell geometry was designed to observe the imbibition for a mixed wet case, as shown in Fig. 2A. Since the production of these cells involves repetitive steps and switching of the setup between experiments should be as quick as possible, multiple cells are produced in each batch. The cells are arranged in parallel in a block of PDMS and can be operated individually. Here, eight cells are placed on a single microfluidic chip (compare Fig. 2B).

The heterogeneous wettability is again established by the combination of an hydrophilic and hydrophobic material. Additionally different constriction widths appear in the microfluidic chip. The hydrophilic wall fraction in the feature area is 40 %, the hydrophobic wall fraction is 60 %. The pillars have different radii ranging from 89 µm to 249 µm. Between the pillars, there are in total 22 constrictions ranging from 68 µm to 341 µm. This is, for manufacturing reasons, one order of magnitude larger, than in real porous gas-diffusion electrodes (Franzen et al., 2019). Like in the real porous system, there are constrictions of different wettability in the system. A fully measured schematic is given as Supporting Information S1.

2.3. Fabrication of microfluidic chip

To represent the non-wetting PTFE and wetting metal phase often used in a real GDE, some simplifications were made. Whereas in GDEs for oxygen reduction the metal (i.e. silver) is the hydrophilic phase and PTFE is the hydrophobic phase, here we use PDMS as the hydrophobic phase and an acrylate as the hydrophilic one. The solid phases consist of the hydrophobic polymers PDMS and the hydrophilic poly(hydroxyethyl-co-diethylene glycol acrylate) (hereafter termed simply “acrylate”). The chip itself consists of hydrophobic polydimethylsiloxane (PDMS). To integrate the hydrophilic surfaces, pillar structures are printed into the chip consisting of the acrylate polymer. The liquid phases are represented by water and the perfluorinated polymer Fluorinert FC-770. This enables for easier fabrication of experimental models and more controlled experiments. Using a liquid instead of a gas makes DNS simulations of the systems more efficient, since the density differences are low. Additionally, we were able to reproduce contact angles comparable to those present in a real gas diffusion electrode. The properties of the used materials is given in Supporting Information S2 in Table S1.

The microfluidic model GDE was fabricated using replica molding and photolithography. First, the previously designed channel structure was converted into a negative master structure. The hydrophobic parts were 3D printed with a Nanoscribe Photonic Professional GT+ two-photon lithography 3D printer using IP-S resin obtained from Nanoscribe GmbH. Poly(dimethylsiloxane) (PDMS) was used to cast channels from the printed masters. Sylgard 184 silicone elastomer and crosslinker kits were used in a 1:10 ratio of crosslinker to elastomer base. PDMS was cast over the masters, degassed in a vacuum for 1 h, and cured in a 55 °C oven for at least 4 h. Afterward, access holes were punched into the inlet and outlet channels using 1.2 mm biopsy punches. The PDMS parts were cleaned using isopropanol and plasma-bonded to PDMS-coated glass slides. For oxygen plasma bonding, a Diener Zepto plasma oven was used. To produce the hydrophilic pillars in the chip, a custom UV-curing resin was prepared. It consists of hydroxyethyl acrylate as monomer and diethylene glycol diacrylate as crosslinker in a volumetric ratio of 2:3. Lithium-phenyl-2,4,6-trimethylbenzoylphosphinate (LAP) was used as the initiator at $2\,mg\,mL^{-1}$. A photolithography device (Wolff et al., 2019) was used to print hydrophilic pillars in the chip. Masks were designed using Inkscape version 0.92 and printed onto acetate transparency sheets using a commercial inkjet printer. Chips were filled with the acrylate monomer solution and exposed to UV light through the mask for 1 s at 600 mA power to the 365 nm LED in the photolithography device. For more details on the lithography device, we refer to the original publication (Wolff et al., 2019). After polymerization, non-polymerized resin was flushed out using isopropanol. The chips were dried and stored for at least 3 d to ensure that the plasma-activated PDMS surface returns to a hydrophobic state (Maier et al., 2024).

2.4. Contact angle measurements

The contact angles of all substances were measured in two different ways: (1) in a chip filled with both fluids and (2) in a specially constructed chamber to allow measurement of contact angles on flat surfaces against fluids different than air; in our case, Fluorinert and water. (1) For measurements in a chip, a channel was filled with water. Then, a small amount of FC-770 was pumped into the chip until several phase boundaries between the two phases developed in the pore network. From a microscopy image, the contact angles of the phase boundary on different parts of the channel were evaluated. For that, lines were fitted to the phase boundaries at the point of contact with a solid surface and the angle between the lines was measured (compare Fig. 3A). At least five points were evaluated for each pairing of solids and fluids to obtain the standard deviation between the measurements. (2) For additional measurements, a chamber was constructed from PDMS-coated glass slides. Here, planar surfaces were used as the substrate to characterize the contact angle without any influence from the microfluidic channel (compare Fig. 3B). This allowed the observation of a droplet of water in air or in a continuous phase of FC-770 on the PDMS surface. The contact angle was evaluated from photographs and with a Krüss DSA100 contact angle measuring device.

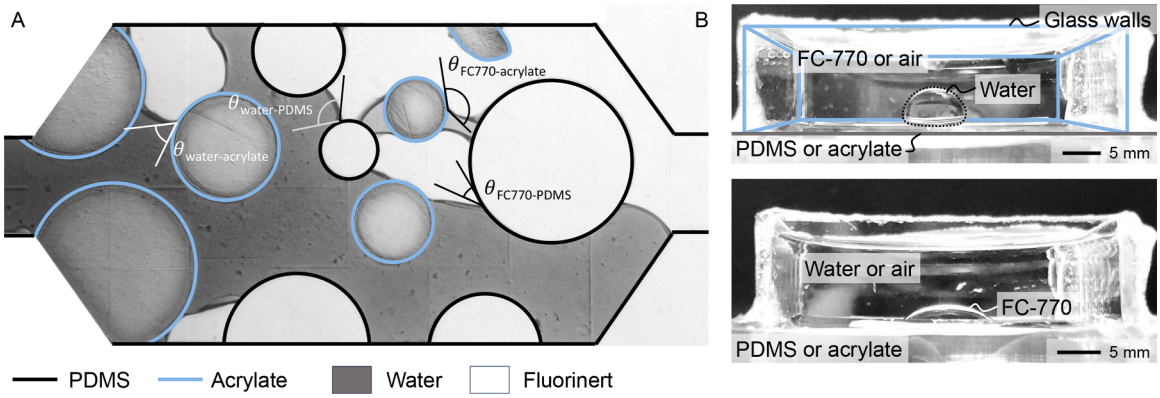

Fig. 3. Measurement of contact angles between fluids. A: Exemplary in-chip measurement. B: Photographs of measurement against different continuous phases. The measurements were done for PDMS and acrylate surfaces in the combinations given in the figure.

Table 1
Contact angles including standard deviation of FC-770 and water on PDMS and acrylate. The surface tension between water and FC-770 is 44 mN m^{-1} (Huang et al., 2022).

Property	PDMS	Acrylate
Water contact angle against FC-770 [°]	109.9 ± 10.7	62.6 ± 12.0
FC-770 contact angle against water [°]	70.07 ± 12.1	117.40 ± 10.8

All contact angle measurements showed a material-dependent distribution. Variations of up to 15° were observed for Fluorinert on PDMS against air as well as water. This could also be estimated by comparing contact angle measurements in the microfluidic chip and on a flat external surface.

Within the chip, the surface of the PDMS is likely less smooth since the master structure it is molded from has nanoscale roughness due to the fabrication process, "tiling" (as can be seen in all microscopy images). On the cast, flat surfaces, the water contact angles are on average slightly higher on PDMS. Similar trends were observed for acrylate, which seems to form a smoother surface when printed in larger areas, leading to lower water contact angles. The mean contact angles, including the standard deviation, are given in Table 1. Contact angles were measured on either PDMS or acrylate surfaces. A water droplet surrounded by Fluorinert FC-770 (hereafter, "water contact angle against FC-770") and an FC770 droplet surrounded by water (hereafter, "FC-770 contact angle against water") were measured. The top and bottom of the microfluidic chip consist of PDMS, so all relevant contact angles are captured by the values in Table 1. All other fluid properties of water (Haynes et al., 2016; Dean, 1999) and Fluorinert FC-770 (FC770, 2019) were taken from the literature and material data sheets and can be found in Supporting Information S2.

2.5. Wetting experiments

For a typical experiment, a microfluidic chip was placed under a microscope with tubing attached to each side. An Elveflow OB1 microfluidic flow controller is used to pump the different fluids into the chip. On each side, valves are placed in the tubing to remove any trapped air bubbles. First, the chip is fully filled with water. For better observability, the water is dyed dark blue (0.1 mg mL^{-1} toluidene blue). Then, after all air bubbles are removed from the tubing, the FC-770 is slowly pumped toward the inlet channel of the chip. When a stable phase boundary is established, the current pressure difference is noted from the sensors of the flow controllers. Since the liquid is pumped into the channel from above, a certain constant hydrostatic pressure is present. Thus, the applied and measured pressures are relative to the initial pressure difference. Then, the pressure on the FC-770 side is increased in increments of 50 Pa. Each pressure step is kept until no movement of the phase boundary can be detected for 20 s. To characterize flow behavior, the capillary number can be calculated as the ratio of viscosity and characteristic velocity to interfacial tension. For our system, a value in the order of magnitude of 10^{-9} is calculated, showing that the flow behavior is mainly defined by capillary forces. The capillary number Ca is defined as the ratio of viscosity η and flow velocity v to the surface tension between the two phases γ_{wn}. Since the viscosities of the used fluids are very close to each other, we chose to use the averaged value for an estimation of Ca:

$$Ca = \frac{\eta v}{\gamma_{wn}} = \frac{\left(\frac{1+1.359}{2}\right)\mathrm{Pa\,s} \cdot 2.5\,\mathrm{m\,s^{-1}}}{0.044\,\mathrm{N\,m^{-1}}} = 6.7 \cdot 10^{-9} \quad (1)$$

The fluid flow velocity was measured from videos of the experiment by recording the time the liquid-liquid phase boundary traveled a defined distance of 100 µm and cross-referenced with measurements of volume flow at the outlet. Volume flow was converted to velocity by dividing by the cross-sectional area of the channel at the location of the phase boundary. Velocities were measured at different locations in the channel. Values between 15 µm min^{-1} to 600 µm min^{-1} were obtained, resulting in a range of Ca from $2.7 \cdot 10^{-7}$ to $6.7 \cdot 10^{-9}$. Mostly, low velocities were measured, so on average, the capillary number was in the range of $1 \cdot 10^{-9}$.

For an accurate comparison with simulations, exact sensor placement is important. The length of the tubing between the sensor and the chip was the same for the inlet and outlet, and the sensors were placed at the same height as the channel to exclude hydrostatic effects. The entire experiment is recorded, and from the video, all relevant data in addition to the pressure is obtained.

2.6. Image processing

A Matlab script was written to automatically evaluate the recorded experimental videos. First, the moving phase boundary is isolated using background removal. Then, the original video is converted into frames at defined intervals, and each RGB frame is split into the individual color channels. Different thresholds isolate different parts of the result: the water phase is isolated and different fluid-solid boundaries can be detected. From these images, the water saturation and different fluid-solid interfaces are then extracted. In this work, interfaces of water with different solid walls are shown, since the hydrophilic boundaries and the water phase could be detected more reliably than the hydrophobic phases.

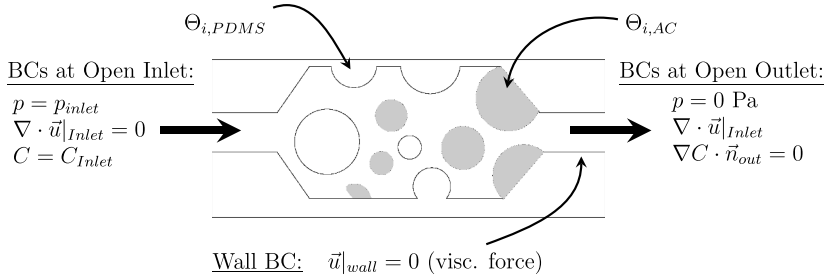

Fig. 4. Boundary conditions and relevant parameters for the full micromodel simulation.

3. Numerical model

3.1. Model equations

To describe the flow field inside the artificial GDE, we assume an isothermal and incompressible multi-phase flow field in a continuous domain. The continuity for the incompressible system is satisfied by the divergence-free velocity field

$$\frac{d\rho}{dt} = -\rho(\nabla \cdot \vec{v}) = 0 \tag{2}$$

The momentum balance can be described by the incompressible Navier-Stokes-equation. Its Lagrangian formulation reads as

$$\rho \frac{d\vec{v}}{dt} = -\nabla p + \mu \nabla^2 \vec{v} + \rho \vec{g} + \vec{f}_{wn} + \vec{f}_{wns} \tag{3}$$

∇p is the pressure gradient, $\mu \nabla^2 \vec{v}$ is the viscous force for a Newtonian fluid and $\vec{g}$ is a body force like gravity acting on the fluid. Because of the small Bond-number ($Bo \approx |\vec{f}_g|/|\vec{f}_{wn}| \approx {}^{\Delta\rho\, g H^2}/_{\gamma_{wn}} \approx 1.4 \cdot 10^{-3}$), we neglect gravity here. $\vec{f}_{wn}$ is the force acting at the surface between the two-liquid phases and $\vec{f}_{wns}$ is the force acting on the triple point (in 2D) between the liquid phases and the solid phases.

3.2. Boundary and initial conditions

Fig. 4 shows the boundary conditions applied for the microfluidic models. The pressure difference over the domain was enforced using Dirichlet pressure boundary conditions at the inlet and outlet of the domain. At the inlet, a fluid (water or Fluorinert FC770) was able to enter the domain, while at the outlet, both liquids can leave the domain. In the calculation of the viscous force at all walls, a no-slip boundary condition is applied. For the initial filling, a straight liquid-liquid interface was set into the inlet channel and relaxed to its initial state. For further pressure increments, the liquid distribution of the last pressure step was chosen as the initial condition for the next stage. All pressure steps were run until a stationary flow field was reached.

3.3. Smoothed particle hydrodynamics model

To discretize the flow equations, the Smoothed Particle Hydrodynamics (SPH) method was used. SPH, developed by Gingold (1977), Monaghan (1992), was chosen due to its mesh-free nature, which allows to capture the large interface deformations that occur in the system. A recent review of the current state of the method can be found in Shadloo et al. (2016). The SPH method is based on the approach of obtaining a quantity $A(r)$ by a weighted integral interpolation of the quantities $A(r')$ over a region Ω

$$A(r) = \int_{\Omega} A(r')\, W(r - r', h)\, dr' \tag{4}$$

As weighting or kernel function, we used the C2-Spline-Kernel from Wendland (1995), which has compact support and according to the analysis by Szewc et al. (2012), showed less tendency to agglomerate particles compared to other spline functions.

The smoothing length or cutoff radius h as a scaling parameter was chosen as $h = 5.2 \cdot l_0$, with l_0 being the resolution used initially. The method for correcting the kernel and the kernel gradient derived by Bonet and Lok (1999) from a calculus of variations is used for all the kernels shown in this work to improve consistency and convergence. Therefore in the following sections, the abbreviation $\tilde{\nabla} \tilde{W}_{ij} = \mathbf{L}_i \nabla \tilde{W}_{ij}$ with the correction matrix $\mathbf{L}_i$ as described byBonet and Lok (1999) will be used.

To discretize the flow equations, the model proposed by Hu and Adams (2007) with its inter-particle averaged spatial derivatives was used. The viscous term, formulated by Morris et al. (1997) includes the fluid-fluid interaction of the interior particles N_f and the fixed solid wall particles N_s. The inter-particle averaged formulation (Hu and Adams, 2007) was used:

$$\begin{aligned}\left(\nu \nabla^2 \vec{v}\right)_i = &\frac{1}{m_i} \sum_j^{N_f} \overline{\mu}_{ij} \left(\frac{m_i^2}{\rho_i^2} + \frac{m_j^2}{\rho_j^2}\right) \frac{\vec{r_{ij}}}{|\vec{r_{ij}}|^2} \tilde{\nabla}_i \tilde{W}_{ij}\ \vec{v_{ij}} \\ &+ \frac{1}{m_i} \sum_j^{N_s} \mu_i \left(\frac{m_i^2}{\rho_i^2} + \frac{m_j^2}{\rho_j^2}\right) \beta_{ij} \frac{\vec{r_{ij}}}{|\vec{r_{ij}}|^2} \tilde{\nabla}_i \tilde{W}_{ij}\ \vec{v_{ij}}\end{aligned} \tag{5}$$

where $\overline{\mu}_{ij} = {}^{(2\mu_i \mu_j)}/_{(\mu_i + \mu_j)}$ and $v_{ij} = v_i - v_j$ and $\beta_{ij} = \min\left(\beta_{\max},\ 1 + \frac{d_{s,j}}{d_i}\right)$. $\vec{r}_{ij}$ is the inter-particle distance vector. d_i is the wall distance of the fluid particle i and $d_{s,j}$ is the wall distance of the interacting solid particle j and calculated as shown in Kunz et al. (2016a). Following the approach of Hu and Adams (2007) the pressure force in Eq. (3) was discretized as

$$-\left(\frac{1}{\rho} \nabla p\right)_i = -\frac{1}{m_i} \sum_j \left(\frac{m_i^2}{\rho_i^2} + \frac{m_j^2}{\rho_j^2}\right) \overline{p}_{ij} \tilde{\nabla}_i \tilde{W}_{ij} \tag{6}$$

where $\overline{p}_{ij} = {}^{\rho_i p_j - \rho_j p_i}/_{\rho_i + \rho_j}$. For a micro-capillary flow, the physically meaningful modeling of surface forces in SPH is crucial. In our mixed-wet, capillary-force dominated flow regime, two additional forces appear. The Continuum Surface Force (CSF) model, originally introduced by Brackbill et al. (1992) and transferred to the SPH method by Morris (2000) and Huber et al. (2016) uses a volume reformulation of the interfacial boundary condition at the fluid-fluid interface. This results in a reformulated force per volume that acts near this interface with surface tension γ_{wn}:

$$\vec{f}^{VOL}_{CSF,wn,i} = \mathbf{f}_{CSF,wn,i} \delta_{wn,i} = \gamma_{wn} \kappa_{wn,i} \vec{n}_{wn,i}\ . \tag{7}$$

where the curvature $\kappa_{wn,i}$ and normal vector $\vec{n}_{wn,i}$ were calculated with the color function as described in Adami et al. (2010). With this formulation, the normal vector in Eq. (7) was calculated by using c_w and c_n as values for wetting and non-wetting phase particles

$$\vec{n}_{wn,i} = \frac{1}{|c_w - c_n| \frac{m_i}{\rho_i}} \sum_j^{N_f} \overline{c}_{ij} \left(\frac{m_i^2}{\rho_i^2} + \frac{m_j^2}{\rho_j^2}\right) \tilde{\nabla} \tilde{W}_{ij} \tag{8}$$

with $\overline{c}_{ij} = {}^{(\overline{\rho}_i c_j + \overline{\rho}_j c_i)}/_{\overline{\rho}_i + \overline{\rho}_j}$. The curvature $\kappa_{wn,i}$ between the two phases was then calculated by using the divergence of the unit normal vector $\hat{\vec{n}}_{wn} = {}^{\vec{n}_{wn}}/_{|\vec{n}_{wn}|}$ as

$$\kappa_{wn,i} = -\nabla_i \cdot \hat{\vec{n}}_{wn,i} = -\sum_j^{N_e} \frac{m_j}{\rho_j} \left(\hat{\vec{n}}_{wn,j} - \hat{\vec{n}}_{wn,i}\right) \cdot \tilde{\nabla}_i \tilde{W}_{ij} \tag{9}$$

For the interface curvature calculation, only particles whose normal vector exceeds the amount

$$|\vec{n}_{wn,i}| > \epsilon = \frac{0.01}{h}\frac{2\rho_i}{\rho_w + \rho_n} \tag{10}$$

were taken into account. The same procedure as for the fluid-fluid interface can be applied for the force acting at the triple point between the wetting, non-wetting, and solid triple point. The volume formulation as described in Huber et al. (2016) reads

$$\vec{f}^{VOL}_{CLF,wns,i} = \gamma_{wn}\left(\cos\Theta_{E,i} - \cos\Theta_{D,i}\right)\hat{\vec{v}}_{ns}\delta_{nws,i} \tag{11}$$

$\delta_{nws,i}$ is the volume reformulation parameter and $\hat{\vec{v}}_{ns}$ is the normalized vector, which points from the contact line or point (in 2D) into the direction of the phase interface ns as described in the aforementioned work.

$$\hat{\vec{v}}_{ns,i} = |\vec{d}_i|^2\,\vec{n}_{wn,i} - \left(\vec{d}_i \cdot \vec{n}_{wn,i}\right)\vec{d}_i. \tag{12}$$

The distance vector $\vec{d}_i$ (and its normalized form $\hat{\vec{d}}_i$) is a vector that points in the direction of the next wall.

$$\delta_{nws,i} = -2\hat{\vec{d}}_i \cdot \sum_j^{N_\epsilon}\left(\delta'_{nws,i} - \delta_{nws,i}\right)\tilde{\nabla}\tilde{W}_{ij} \tag{13}$$

with

$$\delta'_{nws,i} = \begin{cases} \hat{\vec{v}}_{ns,i}\cdot\hat{\vec{n}}_{wn,i} & \text{for } j \in N_{f,s} \\ 0 & \text{for } j \in N_{i,s} \end{cases} \tag{14}$$

According to Kunz et al. (2020) a calculation of the contact angle in mechanical equilibrium $\Theta_{E,i}$ in the case of a wall consisting of differently wettable phases can be done for the fluid particles as

$$\cos\Theta_{E,i} = \frac{1}{\gamma_{wn}}\frac{\sum_j^{N_{s,i}} m_j/\rho_j \gamma_{ws_k,j} W_{ij}}{\sum_j^{N_{s,i}} m_j/\rho_j W_{ij}} \tag{15}$$

This ensures a smooth transition for the contact angle, dependent on the surface tension $\gamma_{ws_k,j}$. The wall particles s_k can have different values for the different solid wall phases. The dynamic contact angle $\Theta_{D,i}$ was calculated from the model of Huber et al. (2016) with modifications of Kunz et al. (2020) from a volume-reformulated weighted summation:

$$\cos\Theta_{D,i} = -\sum_j^{N_\epsilon}\frac{m_j/\rho_j \delta_{wns,j}\hat{\vec{d}}_j\hat{\vec{n}}_{wn,j}}{m_j/\rho_j\delta_{wns,j}} \tag{16}$$

Here, $\hat{\vec{d}}_j$ is the normalized distance vector that points in the direction of the next wall.

The inflow and outflow boundary conditions described in Section 3.2 were implemented using the mirror-particle approach of Kunz et al. (2016a), an improved version of the open boundary conditions applied by Hirschler et al. (2016) with a fixed mirror axis. At the inlet, SPH particles of the inlet phase (water or Fluorinert FC770) were injected at the domain, while at the outlet, all particle colors were able to leave the domain. The no-slip wall boundary conditions were implemented using the approach by Morris et al. (1997) with the calculation of the wall distance for arbitrarily shaped walls as described by Kunz et al. (2016a).

For time-stepping, we enforced both a divergence-free and a density-invariant incompressible SPH (DFDI-ISPH) scheme, as shown in Xu et al. (2009). This scheme is based on the projection method from Cummins and Rudman (1999) with the extensions proposed by Hu and Adams (2007) to get a volume-conservative scheme due to the solution for the particle position. Additionally, the particle shifting procedure from Xu et al. (2009) was applied, but with only one shifting procedure per time step. At the fluid and solid interfaces, only a tangential shifting was applied, to not artificially move the interface and the triple point.

3.4. Reduction to a 2D + 1D model

In contrast to complex porous media, where the relevant features can vary in all spatial directions, in our model, the relevant features with respect to fluid flow vary in only two coordinate directions. To focus on wettability in the flow direction and reduce the computational load, we reduced the model to a *2D + 1D* representation. A validation of this model reduction and a direct comparison against the *full 3D* solution is given in Section 4.1. The most relevant factor for three-dimensional wetting phenomena is caused by wetting induced by corners.

The criteria for spreading corner flow, derived by Concus and Finn (1969) can be extended to corners consisting of two different solid materials (Concus and Finn, 1994). In this case, the condition for wetting in our system then reads

$$\Theta_{PDMS} + \Theta_{Acrylate} < \pi - \alpha \tag{17}$$

with Θ being the contact angle of water against the solid material and α is the corner angle between the two adjacent walls. As it follows from Eq. (17), using the contact angles given in Table 1, the water-Flourinert system would not be able to fully spread into a PDMS-acrylate corner above corner angles of 7.5°. Since our right-angled corner should have an angle of $\alpha = \frac{1}{2}\pi \equiv 90°$, no cornerflow should occur in our setup. Further discussion on the appearance of corner flow and its calculation in a 3D model geometry with SPH is given in Supporting Information S6.

A formulation of the entry pressure p_{fill} for the main meniscus in straight polygonal cross-sections was derived using the MS-P theory (Mayer and Stowe, 1965; Princen, 1969) by Lago and Araujo (2001). Corner-flow was assumed in their model. The special case of our rectangular channel can be written as:

$$p_{fill} = -2\cdot\gamma_{wn}\left(\frac{1}{W_{app}} + \frac{1}{H_{app}}\right) \times\left(\cos\Theta + \sqrt{cos\Theta^2 - \frac{H_{app}W_{app}}{\left(H_{app}+W_{app}\right)^2}f_T(\Theta)}\right) \tag{18}$$

with function

$$f_T(\Theta) = \left[4\cos\Theta(\cos\Theta - \sin\Theta) - (\pi - 4\Theta)\right], \tag{19}$$

where Θ here is the contact angle of FC-770 on PDMS. If, as expected, there is no corner flow, the pressure contribution can be split in two independent curvatures, one in flow direction κ_{sim} and one in direction of the top and bottom plate k_{app}. This results in the well-known capillary entry-pressure equation for rectangular ducts (see Lago and Araujo (2001) for the case of same wettability on top and bottom plate, for a detailed discussion on the derivation from Eq. (18) we refer to Blunt (2016)):

$$p_{fill} = -\gamma_{wn}\kappa = -\gamma_{wn}\left(\kappa_{sim} + \kappa_{app}\right) \tag{20}$$

The curvature κ_{sim} is calculated directly by our numerical model (see Section 3.2). In the third dimension, we assume a static contact angle that is identical on both sides. With this assumption, the curvature in the third direction can be calculated as:

$$\kappa_{app} = \frac{2\cos(\Theta_{PDMS})}{H_{app}} \tag{21}$$

where Θ_{PDMS} is the static contact angle between water and the PDMS surface, and H_{app} is the distance between the top and bottom plates. Subsequently, a constant pressure $p_{app} = -\gamma_{wn}\kappa_{app}$ has to be added to the numerically evaluated pressure p_{sim} to account for the third dimension:

$$p_{fill} = p_{sim} + p_{app} = p_{sim} \underbrace{-2\gamma_{wn}\frac{\cos(\Theta_{PDMS})}{H_{app}}}_{\substack{p_{app} = 333\,\text{Pa for single pore micromodel} \\ p_{app} = 300\,\text{Pa for full micromodel}}} \tag{22}$$

From this calculation, one can see the additional overpressure resulting from the curvature in the third dimension, named here as p_{app}. It has

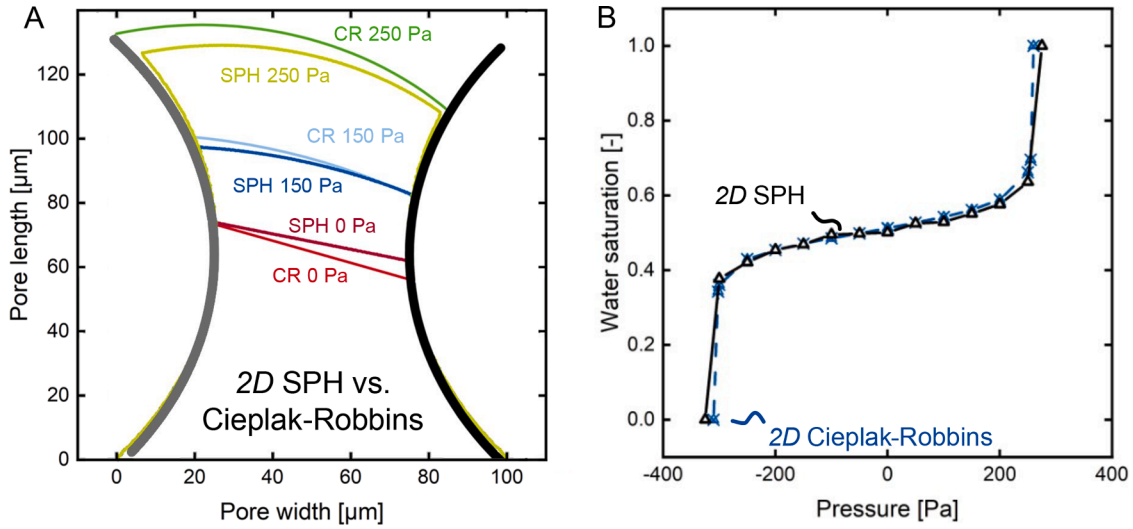

Fig. 5. Comparison of the *2D* SPH and CR models for the mixed-wet water intrusion case. A: Phase boundaries according to the SPH and CR model. 0/0.1 Pa (SPH: dark red/CR: bright red, slight deviation from zero to prevent division by zero in the CR model), 150 Pa (SPH: magenta/CR: blue), and 250 Pa (SPH: bright green/CR: dark green). The hydrophilic side of the pore is shown in gray, the hydrophobic part is black. B: Saturation curve for the single pore model. Water saturation was calculated with SPH (open symbols) and the CR-Model (crossed symbols).

a value of 333 Pa for the single pore micromodel and 300 Pa for the full micromodel due to slightly different H_{app}. Adding this pressure to the simulated *2D* model results in a *2D + 1D* model.

Again, because of the absence of corner flow in our model, we assumed a fully developed laminar flow profile between parallel plates in the third dimension. This analytical solution is well-documented in many fluid mechanics textbooks. To adjust for this dimension reduction, we added an additional viscous force:

$$\frac{d\vec{v}_{red}}{dt} = \frac{d\vec{v}}{dt} - 12\frac{\mu}{\rho H^2}\vec{v} \tag{23}$$

However, this reduced velocity introduces an error that depends on the width-to-height ratio, as shown by Kunz et al. (2016b). Furthermore, the assumption of a parabolic flow profile is not true in the closest region of the capillary surface, where it resembles more like a block profile. Despite the reduced viscous force, the model is unable to predict correct temporal evolution due to other effects such as surface roughness and stick-slip behavior (Kunz et al., 2018) that impact the wetting dynamics.

3.5. Implementation

The presented model is implemented in SiPER (Siper, 2024), an MPI-parallelized free SPH code in C standard language, developed at the University of Stuttgart. The pressure-Poisson equation for both the divergence-free and density-invariant conditions is solved using the BoomerAMG (Henson and Yang, 2002) pre-conditioner from the Hypre library (Hypre, 2024) with *extended + i* parallel interpolation and a damping factor of 0.95 for BoomerAMGs hybrid smoother, AMG strong threshold of 0.25 and the BiCGStab-Solver from the Petsc library (Balay et al., 2023). All calculations were carried out on a Linux cluster that uses Intel Xeon E5-1620 v2 CPUs (3.7 GHz).

3.6. Validation of the mixed-wet direct numerical simulation

The parameter of interest is the entry pressure Δp between the inlet and the outlet of the domain and its influence on the imbibition of the wetting fluid. A study on the discretization error of the breakthrough pressure for a straight 2D channel with a hydrophobic patch can be found in Supporting Information S3.

To prove the correctness of the entry pressure model for a realistic mixed-wet geometry in a defined system, we validated it against an analytical model. The same geometry as shown in Section 2.1 was used.

First, the *2D*-SPH model was compared to an analytical solution. Cieplak and Robbins (1990) developed an analytical geometrical model (CR-Model) to describe the existence and shape of capillary surfaces between two circles of different sizes and wettability in *2D*. The CR model is discussed in detail in Li's work (Li, 2020). In the absence of gravity or temperature gradients, the curvature radius $R = \gamma_{wn}/|\Delta p|$ of a capillary surface depends only on the surface tension γ_{wn} and the pressure difference $|\Delta p|$ between the two fluids. In the CR model, a surface can only exist if it is possible to find a surface that simultaneously fulfills the boundary conditions (i.e. contact angles on the respective circles) for a given radius of curvature R. It is evident that this is not feasible for all given pressures, and the maximum possible pressure is just before the interface becomes unstable and bursts. The CR model is limited to circular geometries, therefore, equilibrium surfaces touching the channel walls aside from the pillars can not be described.

In Supporting Information S4 we give the full description and set of equations used for the CR-model calculations. All data was calculated and extracted with a Python script based on the formulas given there. Fig. 5A shows a direct comparison of the equilibrium profiles calculated by CR and SPH for a differential pressure of 0, 150, and 250 Pa. Clearly, all profiles match very well and deviations are minor. This is supported by the calculation of the full water saturation range of the single pore that is given in Fig. 5B. Here, a mean and a maximum relative deviation in saturation of 1.55 % and 4.50 % between CR and SPH was calculated. This validates the accuracy of our numerical method for the full saturation range in direct comparison with an analytical model.

Second, a *full 3D* SPH simulation was conducted for the single pore model. Fig. 6 shows the filling process of the single mixed-wetting pore. As expected, no corner flow was observed, which confirms the reduction from *full 3D* to *2D + 1D*. Next, the saturation profiles were compared to the *2D + 1D* SPH- and CR-model including the added pressure of p_{app} = 333 Pa, as described in Section 3.4.

As depicted in Fig. 7, the overall course of both *2D + 1D* and *full 3D* model are comparable. The greatest difference are at low water pressures, where first water intrusion was predicted between 18 Pa and 68 Pa depending on the model. For all other points, a mean relative deviation of 3.16 % and a maximum relative deviation in saturation of 5.62 % was

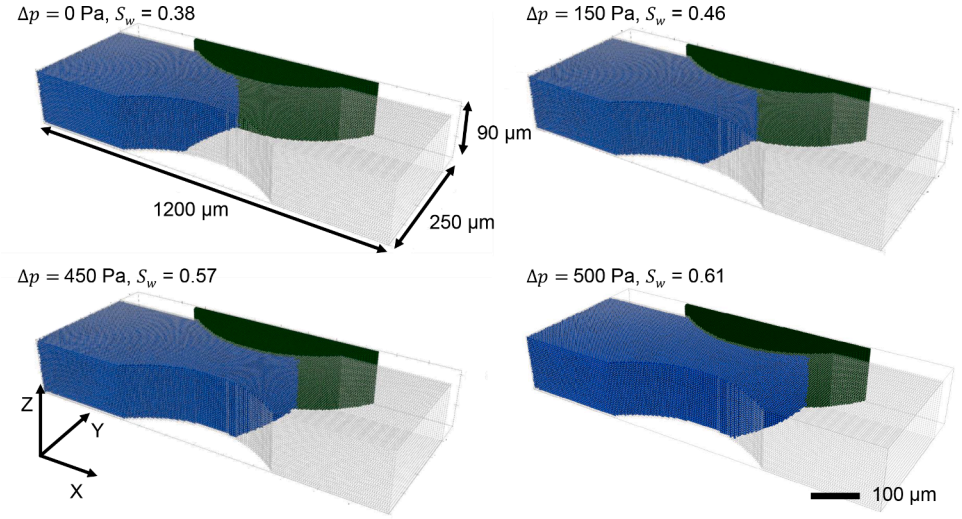

Fig. 6. *Full 3D* simulation of water (blue) displacing FC-770 (transparent/not shown) in the mixed-wet single pore system. The hydrophilic acrylate pillar is shown in green, while all other walls consist of hydrophobic PDMS, colored in transparent gray. The increasing water saturation S_w as a consequence of the increasing water overpressure is shown.

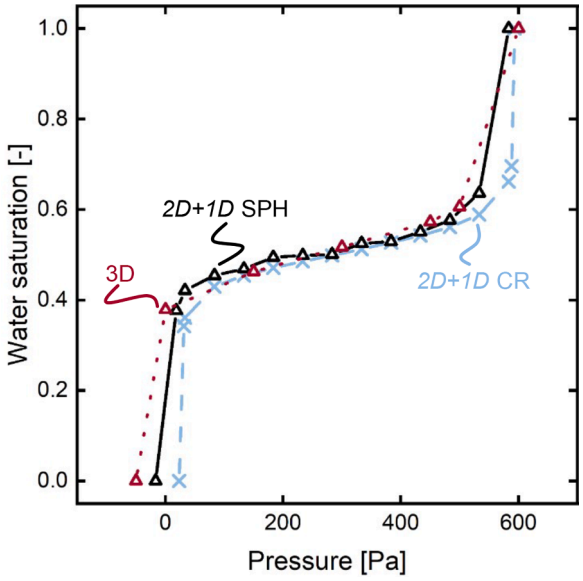

Fig. 7. Comparison of the saturation curve for the *full 3D*, and the *2D + 1D*-SPH model for the mixed-wet water intrusion case.

obtained. From this, we conclude that our *2D + 1D* model can capture the most relevant effects in the mixed-wet pore.

4. Results and discussion

4.1. Single pore imbibition

Numerical simulations of the imbibition of a single mixed-wet pore have been described in Section 3.6. Now the single pore was investigated experimentally. In Fig. 8, the results of the *2D + 1D* SPH simulation and the experiment for the single pore model are shown for water intrusion, i.e. water displaces the Fluorinert phase. In the single-pore experiment, no corner flow was observed.

For a more comprehensive comparison between the experimental and simulated results, the phase boundaries were extracted and plotted at different pressure steps (compare Fig. 9A). Notably, the profiles extracted from experiment and simulation are very similar with a constant offset of approximately 30 Pa. Comparing the water saturation shown in Fig. 9B, the experimental pressure-saturation curve appears to be compressed. Here, a mean and maximum relative deviation of saturation of 5.3 % and 48.6 % (for 500 Pa) between SPH and experiment was calculated. The deviations can be explained by the impreciseness in contact angle, as lined out in Section 2.4. They seem also to differ slightly for the top and bottom plates. Calculating the pressure difference for a change of 10° in the contact angle with the Eq. (20) and (21) results in a difference of about 150 Pa. However, the overall behavior agrees well between experiment and simulation.

4.2. Full pore network

Although the single-pore model is well suited for basic validation, it neglects further interactions. Different pore sizes and ratios of hydrophilic and hydrophobic areas leads to complex capillary fingering during imbibition.

In the experiments, a similar procedure was applied as for single-pore experiments. First, a stable phase boundary was established in the inlet of the structure. Then, the interface was moved through the channel by stepwise pressure increases. Through the transparent top and bottom layer, the saturation could be monitored in detail. In Fig. 10, pressure steps with identical saturation are shown for experiment and the *2D + 1D* SPH simulation.

For pressures below 650 Pa, the fluid-fluid boundary agrees well between experiment and simulation. As the colorless, hydrophobic Fluorinert FC770 is the intruding fluid, we expect that it wets the most hydrophobic accessible pores along its path. Due to the hydrophobic top and bottom plates, all pores with a hydrophilic part are mixed-wetting; for this work, a “mixed” pore has three hydrophobic walls and one hydrophilic wall and a “primarily hydrophilic” pore has two hydrophilic and two hydrophobic walls. This wetting path along the most hydrophobic accessible pores can also be observed in the experiment, with the exception of the breakthrough point at the outlet of the structure. Here, primarily hydrophilic pores are placed. The breakthrough is expected to occur through the mixed-wet pore in the experiment. However, the Fluorinert passes the primarily hydrophilic pore first. In the simulation, the breakthrough at 675 Pa occurs only through the pores at the top of the micromodel (constriction 10 as numbered in Supporting Information S5). This leads to a large trapped water pocket that is no longer able to escape from the simulation domain. In Supporting Information S5 we also give the maximum burst pressure for all constrictions

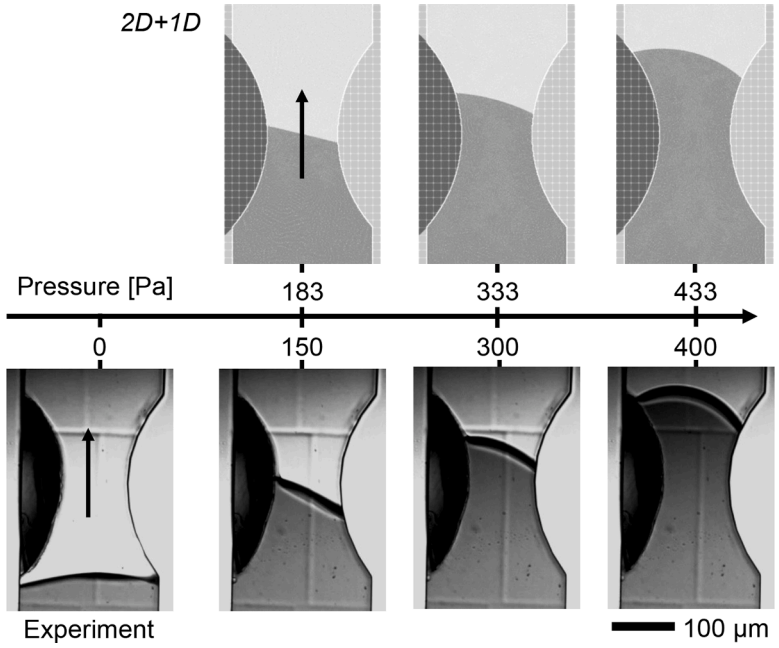

Fig. 8. Comparison of experimental and simulated results for single pore intrusion. Dark gray pillars and areas are hydrophilic, and light gray areas and pillars are hydrophobic. In the shown experiment, water displaces Fluorinert.

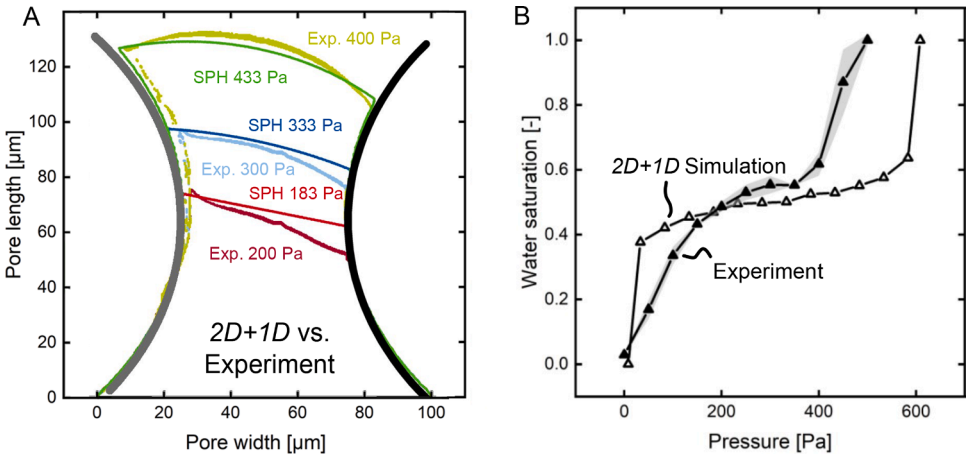

Fig. 9. Comparison of the *2D + 1D* SPH model with experimental data. A: Comparison of SPH and experimentally extracted profiles for 183/200 Pa (SPH: dark red/Exp: bright red), 333/300 Pa (SPH: magenta/Exp: blue), 433/400 Pa (SPH: bright green/Exp: dark green). The hydrophilic side of the pore is shown in gray, and the hydrophobic one in black. Deviations from walls are due to inaccuracies in boundary detection from experimental data. B: Saturation curves extracted from experimental data (closed symbols) and calculated with SPH (open symbols.).

calculated with the CR-Model, which also only considers 2-dimensional effects. Following the path from lowest to highest pressure in the CR model, the same path would also be preferable as in the *2D + 1D*SPH simulations.

Like in a real electrode, our microfluidic system has a certain contact angle distribution that influences the static and dynamic behavior of the system. Especially for the water contact angle versus Fluorinert on PDMS, a variation of up to 15° was measured inside the microfluidic model. Variations in contact angle occur due to chemical heterogeneity (Woodward et al., 2000) or surface roughness (Wenzel, 1936) in the presented system. These effects could be in principle captured by our SPH-model. However, the determination of the local contact angle is only known *post-operando*.

Comparing the saturation curves in Fig. 11A, the curves clearly show the same steps and the same overall course. In particular, the two plateaus that are observed in the experiments are also well reproduced in the simulation, but again the simulated curve seems to be compressed in the x-axis. To quantitatively compare whether the wetting patterns are similar, the fluid-fluid boundaries, as well as the boundaries with the hydrophilic and hydrophobic wall fractions, are calculated and compared in Fig. 11B. Good agreement is observed between most boundaries. The main deviation can be seen for the boundaries between water and the hydrophilic wall fraction, which leads to the assumption that thin films or flooded corners on the hydrophilic pillars are responsible for the deviations between experiments and simulation. These films can either form on the rough surfaces of the pillars or in the corners between pillar and wall. In our experiments, we observed that films formed in both locations. Over time, water crept between pillar and wall, forming a thin layer around and under the perimeter of the pillar. These flooded corners then likely change the wetting properties of the pillar towards a more hydrophilic behavior. In the experimental saturation curve, a plateau between 400 Pa and 800 Pa indicates the primarily

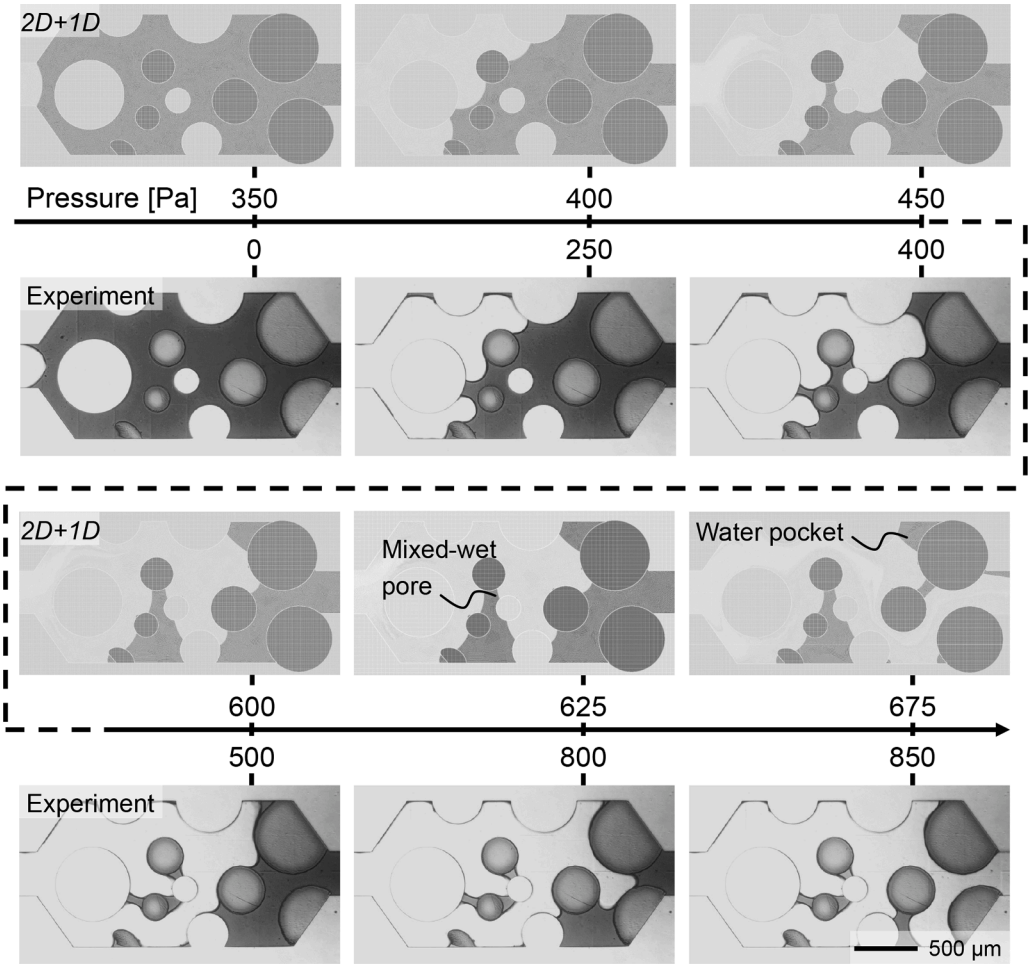

Fig. 10. Comparison of intrusion measurements and simulations for the full model. Dark gray areas are the hydrophilic solid pillars and water, and light gray areas are the hydrophobic solid pillars and Fluorinert FC-770.

hydrophilic outlet area (compare Fig. 11A). In this pressure range, small increases in wetting are due to displacement of water in other regions of the channel, mainly through layer or corner flow. Residual water is drained *via* thin films along the channel walls. Fig. 12 shows a time series of a seemingly trapped water pocket. With increasing pressure difference, the trapped water pocket on the top of the image squeezes out over time. This mechanism can only happen *via* flow in the corners of the domain, neither by mechanical compression nor by dissolution of water in Flourinert. Additionally, a meniscus along the larger pillar can be seen in the images, which indicates the presence of a fluid-fluid boundary in the corner between the pillar and channel walls. Corner flow is likely to happen at strong wetting conditions. The geometric relation at which a corner flow can exist was discussed in Section 3.4. This condition is not fulfilled in our case assuming right angles. Layer or corner flow in multi-phase micromodels was observed by various authors. For example, Zhao et al. (2016) observed a capillary-number dependent corner flow, where wetting layers were formed preferably for low capillary numbers by bypassing the pore body along the points where the pillars meet the top and bottom plate. Recently, Ghiringhelli et al. investigated the cornerflow behavior on plasma-treated PDMS and an epoxy photoresist for a drying process in a micromodel with rectangular corners. Their work indicated, that the treatment and aging of PDMS as an influencing factor to alter the contact angle strongly influences the evolution of corner flow and leads to higher drying dynamics.

Following this insights, one explanation could be local changes to the contact angle due to roughness or the formation of a small gap or lip between pillars and channel top or bottom creating a smaller angle α in our microfluidic model. The latter can be caused during the pillar fabrication within the channel or during closing of the channel. As can be seen in the microscopy images throughout this work, we observed the trapping of water in this lip as a blue ring creeping between the pillar and the channel top. We treat this creeping phenomenon similarly to corner flow, as it follows the same mechanism (discussed in detail in Supporting Information S6). Cornerflow or a formation of thin liquid layers like in Fig. 12 can clearly be observed in the micromodel and seems to be the main effect that is not considered in the SPH simulations. As we showed in Supporting Information S6 it is, in principle, possible to capture the corner flow behavior. However, an appropriate resolution of the wetting layers is beyond the scope of this work. Additionally, it would require knowing the exact geometry, including failures and spatial resolution of small gaps, already *ante-operando*.

The most significant deviation is observed at the breakthrough pressure. In the simulation, a lower breakthrough pressure is calculated. The dimension reduction discussed for the single pore also creates a pressure offset in the full network model. Because the full pore network is more complicated and additional effects such as cornerflow were observed in the experiments, the calculated pressure offset does not fully account for the deviation in the breakthrough pressure. However, the *2D + 1D* SPH model is still valid, as the deviations are caused by experimental inaccuracies. The average deviations between the experimentally measured and simulated values for saturation and phase boundary lengths are 11.4 % and 16.3 %. This indicates an overall very good agreement. As discussed above, the course of the saturation and phase boundaries

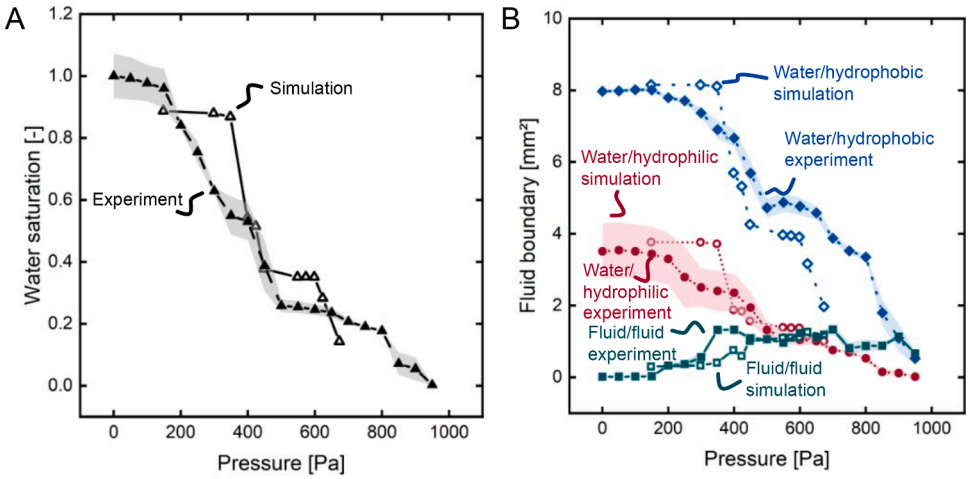

Fig. 11. Comparison of water saturation and phase boundaries for the full pore network model between experiment (filled symbols) and SPH simulations (open symbols). A: water saturation over pressure. B: fluid-fluid and fluid-solid boundaries.

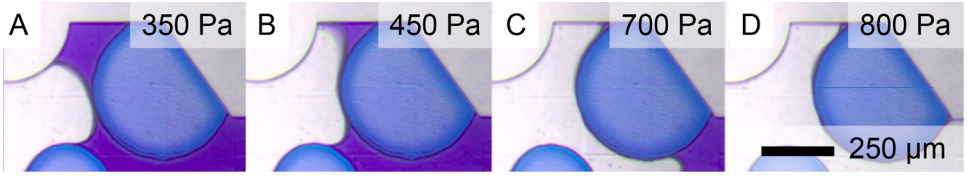

Fig. 12. Sequence of a trapped water pocket, that squeezes out via the corner between pillar and channel wall over time. A: The fluid touches the large hydrophilic pillar (upper right blue pillar). A meniscus is visible that is not seen on the two pillars already wetted with Flourinert (lower left blue pillar). B: A water pocket is trapped in the upper right section. The meniscus is still visible. C: Water squeezes out via the corner between the upper right blue pillar and cover plate. The meniscus radius gets smaller due to the higher pressure difference. D: The corner is drained of any water.

is compressed on the pressure axis for the simulation compared to the experiments. Most notably, the plateaus observed in the experiment extend over a lower pressure range in the simulation. This leads to locally bigger deviations in the range of 300 Pa as here, a major part of the pore network is flooded. Since this major flooding event occurs at a slightly lower pressure in the experiment, deviations are significantly higher for 300 Pa to 350 Pa (maximum deviation 83.1 %). Additionally, the measurement uncertainty of the contact angle may have a significant impact when the pore sizes are in a range where the breakthrough pressure strongly depends on the contact angle. Experimentally, a broad distribution of contact angles, most likely caused by different surface roughness, was observed. Thus, using an average value for the contact angle is an assumption, that yields overall fitting results, but will not capture every detail of the wetting state in every pore. However, considering the flow path of the full micromodel as shown in Fig. 10, the flow path is in overwhelming agreement with the experiment.

Overall, a good agreement was found between SPH modeling and experimental studies of mixed wettability in heterogeneous channel systems. A constant offset factor was found for the dimension reduction, yielding our *2D + 1D* SPH model. The main deviation between the model and the experiment is caused by layer- or cornerflow, which was observed in the experiment but can not be considered in DNS simulations without detailed spatial resolution of the wetting properties between pillars and top and bottom cover plate. In addition, a distribution of contact angles, in contrast to two constant angles, was found in the experiments. Although this accurately describes the behavior of real GDEs, it is difficult to incorporate this into the SPH simulation. Thus, complete quantitative predictions of the electrolyte distribution can not be expected. However, considering the discussed deviations, a good prediction of the wetting behavior of mixed-wetting pore systems can be made and the saturation can be determined with good accuracy. We obtained an average deviation of 16.3 % regarding phase boundaries and 11.4 % for saturation between simulation and experiment. Several other factors could contribute to deviations between the two models. An extensive discussion relating the parameters of our models to real GDEs can be found in Supporting Information S7.

5. Conclusion

In conclusion, an improved SPH simulation for mixed wettability and a novel microfluidic model system to validate the SPH simulation were presented. For the first time, a mixed-wetting structure with comparable wetting conditions to a silver GDE as used by Covestro (Kintrup et al., 2017) or at TU Clausthal (Bienen et al., 2022; Osiewacz et al., 2024) was created. We showed that our SPH method is applicable for this type of structure. By incorporating a physically consistent contact line force model for mixed-wet boundaries, validated both analytically and experimentally, the SPH modeling achieves more accurate prediction of fluid distributions in heterogeneous-wettable microfluidic systems. This enables us to apply our SPH-model to more complex and realistic 3D structures, as the underlying model equations remain the same regardless of the geometry. Moreover, we show that it is possible to create microfluidic structures with tailored wettability. With this model, we can predict the fluid distribution in mixed-wetting GDEs accurately, as shown by the average deviation of 16.3 % regarding phase boundaries and 11.4 % for saturation between simulation and experiment. From the fluid distribution and phase boundaries, conclusions as well as predictions for ideal structures and process conditions can be made. We provide relations between pressure, wettability and saturation, enabling tailored design of GDEs by adjusting e.g. the binder content to change the hydrophobic wall fraction. Moreover, we found that incorporating regions in the catalyst layer with predominantly hydrophilic or hydrophobic surfaces effectively stabilizes the triple-phase boundary over a significant pressure range. The microfluidic model accurately depicts mixed wetting phenomena in a controlled microenvironment. The SPH simulation was validated analytically and experimentally through single-pore intrusion

experiments. It was shown, that the dimension reduction to a *2D + 1D* model is valid and agrees well with the *full 3D* simulation. Cornerflow can in principle be described by our *full 3D* model, but the conditions for it are not fulfilled under the assumption of the designed geometry. The comparison between simulations and experiments, however, revealed the impact of contact angle distribution and of layer- or cornerflow. Both were observed in the more complex experiments due to inhomogeneous surfaces and inaccuracies in the model fabrication. Thus, we conclude that our simulation accurately depicts mixed wettability based on different surface wettabilities and capillary pressures, while the determination and identification of the actual surface conditions on the smallest scale as inputs for the simulation remains an experimental challenge for mixed wetting microfluidics.

Statements & Declarations

Funding

This work was supported by the DFG in the framework of the research unit FOR2397, “Multi-scale analysis of complex three-phase systems: Oxygen and CO_2 reduction at silver-based gas-diffusion electrodes in aqueous electrolyte” (Grant No. NI 932/11-2). M.W. acknowledges DFG funding through the Gottfried Wilhelm Leibniz Award 2019 (WE 4678/12-1). M.W. acknowledges the support through an Alexander-von-Humboldt Professorship and the European Research Council (ERC) under the European Union’s Horizon 2020 research and innovation program (grant agreement no. 694946).

Data availability

Data will be made available on request.

Declaration of competing interest

The authors declare that they have no known competing financial interests or personal relationships that could have appeared to influence the work reported in this paper.

CRediT authorship contribution statement

Sebastian Brosch: Methodology, Software, Validation, Formal analysis, Investigation, Data curation, Writing – original draft, Visualization, Writing – review & editing; **Thorben Mager:** Methodology, Software, Validation, Formal analysis, Investigation, Data curation, Writing – original draft, Visualization, Writing – review & editing; **John Linkhorst:** Writing – review & editing, Supervision, Resources, Project administration, Methodology, Funding acquisition; **Ulrich Nieken:** Writing – review & editing, Software, Resources, Project administration, Methodology, Funding acquisition, Conceptualization; **Matthias Wessling:** Writing – review & editing, Supervision, Resources, Project administration, Methodology, Funding acquisition, Conceptualization.

Acknowledgments

T.M. and U.N. acknowledge DFG funding of the research unit FOR2397, “Multi-scale analysis of complex three-phase systems: Oxygen and CO_2 reduction at silver-based gas-diffusion electrodes in aqueous electrolyte” (Grant No. NI 932/11-2). Our thanks go to all members of the group for fruitful discussions and good cooperation in the context of silver-based-GDEs. M.W. acknowledges DFG funding through the Gottfried Wilhelm Leibniz Award 2019 (WE 4678/12-1). M.W. acknowledges the support through an Alexander-von-Humboldt Professorship and the European Research Council (ERC) under the European Union’s Horizon 2020 research and innovation program (grant agreement no. 694946).

Supplementary material

Supplementary material associated with this article can be found in the online version at 10.1016/j.ces.2025.121465.

Supporting Information S1 shows the full dimensions of the fabricated and simulated micromodel.

Supporting Information S2 contains all relevant material parameters.

Supporting Information S3 gives details on the mesh and resolution study of the SPH model.

Supporting Information S4 are the used model equations for the Cieplak-Robbins model.

Supporting Information S5 contains results of the Cieplak-Robbins model for the full pore network.

Supporting Information S6 contains a discussion of the conditions under which cornerflow can occur in our geometry and confirms the applicability for 3D simulation.

Supporting Information S7 contains a detailed discussion of the applicability and limitations of the presented models.

References

Adami, S., Hu, X.Y., Adams, N.A., 2010. A new surface-tension formulation for multi-phase SPH using a reproducing divergence approximation. J. Comput. Phys. 229 (13), 5011–5021. https://doi.org/10.1016/j.jcp.2010.03.022

Agbalaka, C., Dandekar, A.Y., Patil, S.L., Khataniar, S., Hemsath, J.R., 2008. The effect of wettability on oil recovery: a review. In: SPE Asia Pacific Oil and Gas Conference and Exhibition. SPE. https://doi.org/10.2118/114496-MS

Alhammadi, A.M., AlRatrout, A., Singh, K., Bijeljic, B., Blunt, M.J., 2017. In situ characterization of mixed-wettability in a reservoir rock at subsurface conditions. Sci. Rep. 7 (1), 10753. https://doi.org/10.1038/s41598-017-10992-w

Anderson, W.G., 1987. Wettability literature survey Part 5: the effects of wettability on relative permeability. J. Pet. Technol. 39 (11), 1453–1468. https://doi.org/10.2118/16323-PA

Balay, S., Abhyankar, S., Adams, M.F., Benson, S., Brown, J., Brune, P., Buschelman, K., Constantinescu, E.M., Dalcin, L., Dener, A., Eijkhout, V., Faibussowitsch, J., Gropp, W.D., Hapla, V., Isaac, T., Jolivet, P., Karpeev, D., Kaushik, D., Knepley, M.G., Kong, F., Kruger, S., May, D.A., McInnes, L.C., Mills, R.T., Mitchell, L., Munson, T., Roman, J.E., Rupp, K., Sanan, P., Sarich, J., Smith, B.F., Zampini, S., Zhang, H., Zhang, H., Zhang, J., 2023. PETSc Web page. https://petsc.org/.

Bandara, U.C., Tartakovsky, A.M., Oostrom, M., Palmer, B.J., Grate, J., Zhang, C., et al., 2013. Smoothed particle hydrodynamics pore-scale simulations of unstable immiscible flow in porous media. Adv. Water Resour. 62, 356–369. https://doi.org/10.1016/j.advwatres.2013.09.014

Bechtel, S., Crothers, A.R., Weber, A.Z., Kunz, U., Turek, T., Vidaković-Koch, T., Sundmacher, K., et al., 2021. Advances in the HCl gas-phase electrolysis employing an oxygen-depolarized cathode. Electrochim. Acta 365, 137282. https://doi.org/10.1016/j.electacta.2020.137282

Bienen, F., Paulisch, M., Mager, T., Osiewacz, J., Nazari, M., Osenberg, M., Ellendorff, B., Turek T. , Nieken, U., Manke, I., Friedrich, K.A., 2022. Investigating the electrowetting of silver–based gas–diffusion electrodes during oxygen reduction reaction with electrochemical and optical methods. Electrochem. Sci. Adv. . https://doi.org/10.1002/elsa.202100158

Błaszczyk, M.M., Przybysz, Ł., Budzyń, A., 2024. The influence of the variable wettability characteristics of layers on the transport of nanoparticles in the context of drug delivery in skin structures. Int. J. Mol. Sci. 25 (9), 4665. https://www.mdpi.com/1422-0067/25/9/4665. https://doi.org/10.3390/ijms25094665

Blunt, M.J., 2016. Multiphase Flow in Permeable Media. Cambridge University Press, Cambridge. https://doi.org/10.1017/9781316145098

Bonet, J., Lok, T.S.L., 1999. Variational and momentum preservation aspects of smooth particle hydrodynamic formulations. Comput. Methods Appl. Mech. Eng. 180 (1–2), 97–115. https://doi.org/10.1016/S0045-7825(99)00051-1

Brackbill, J.U., Kothe, D.B., Zemach, C., 1992. A continuum method for modeling surface tension. J. Comput. Phys. 100 (2), 335–354. https://doi.org/10.1016/0021-9991(92)90240-Y

Brosch, S., Wiesner, F., Decker, A., Linkhorst, J., Wessling, M., et al., 2024. Spatiotemporal electrowetting and reaction monitoring in microfluidic gas diffusion electrode elucidates mass transport limitations. Small https://doi.org/10.1002/smll.202310427

Burdyny, T., Smith, W.A., 2019. CO 2 reduction on gas-diffusion electrodes and why catalytic performance must be assessed at commercially-relevant conditions. Energy Environ. Sci. 12 (5), 1442–1453. https://doi.org/10.1039/C8EE03134G

Cieplak, M., Robbins, M.O., 1990. Influence of contact angle on quasistatic fluid invasion of porous media. Phys. Rev. B 41 (16), 11508–11521. https://doi.org/10.1103/PhysRevB.41.11508

Concus, P., Finn, R., 1969. On the behavior of a capillary surface ina wedge. Proc. Natl. Acad. Sci. 63 (2), 292–299. https://doi.org/10.1073/pnas.63.2.292

Concus, P., Finn, R., 1994. Capillary surfaces in a wedge: differing contact angles. Microgravity Sci. Technol. 7 (2), 152–155.

Cummins, S.J., Rudman, M., 1999. An SPH projection method. J. Comput. Phys. 152 (2), 584–607. https://doi.org/10.1006/jcph.1999.6246

Dean, J.A., 1999. Lange's Handbook of Chemistry. McGraw-Hill, Inc., New York, St. Louis, St. Francisco. 15 edition.
FC770, 2019. 3m fluorinert electronic liquid FC-770 technical data. https://multimedia.3m.com/mws/media/471785O/3m-fluorinert-electronic-liquid-fc770-product-info-sheet-en.pdf. Online; accessed 8 October 2024.
Franzen, D., Ellendorff, B., Paulisch, M.C., Hilger, A., Osenberg, M., Manke, I., Turek, T., et al., 2019. Influence of binder content in silver-based gas diffusion electrodes on pore system and electrochemical performance. J. Appl. Electrochem. 49 (7), 705–713. https://doi.org/10.1007/s10800-019-01311-4
Gingold, R.A., 1977. Smoothed particle hydrodynamics-theory and application to non-spherical stars. Mon. Not. R. Astron. Soc. 181, 375–389. http://adsabs.harvard.edu/full/1977MNRAS.181.375G.
Haynes, W.M., Lide, D.R., Bruno, T.J. (Eds.), 2016. CRC Handbook of Chemistry and Physics. CRC Press, Boca Raton. https://doi.org/10.1201/9781315380476
Henson, V.E., Yang, U.M., 2002. BoomerAMG: a parallel algebraic multigrid solver and preconditioner. Appl. Numer. Math. 41 (1), 155–177. https://doi.org/10.1016/S0168-9274(01)00115-5
Hirschler, M., Kunz, P., Huber, M., Hahn, F., Nieken, U., et al., 2016. Open boundary conditions for ISPH and their application to micro-flow. J. Comput. Phys. 307, 614–633. https://doi.org/10.1016/j.jcp.2015.12.024
Hu, X.Y., Adams, N.A., 2006. A multi-phase SPH method for macroscopic and mesoscopic flows. J. Comput. Phys. 213 (2), 844–861. https://doi.org/10.1016/j.jcp.2005.09.001
Hu, X.Y., Adams, N.A., 2007. An incompressible multi-phase SPH method. J. Comput. Phys. 227 (1), 264–278. https://doi.org/10.1016/j.jcp.2007.07.013
Huang, H., Xu, W., Wang, Y., Wang, X., He, X., Tong, P., 2022. Fluctuation-induced slip of thermal boundary layers at a stable liquidliquid interface. J. Fluid. Mech. 951, A10. https://doi.org/10.1017/jfm.2022.846
Huber, M., Keller, F., Säckel, W., Hirschler, M., Kunz, P., Hassanizadeh, S.M., Nieken, U., et al., 2016. On the physically based modeling of surface tension and moving contact lines with dynamic contact angles on the continuum scale. J. Comput. Phys. 310, 459–477. https://doi.org/10.1016/j.jcp.2016.01.030
Hypre, 2024. *hypre*: High performance preconditioners. https://llnl.gov/casc/hypre, https://github.com/hypre-space/hypre. Online, accessed 8 October 2024.
Kalde, A., Lippold, S., Loelsberg, J., Mertens, A.-K., Linkhorst, J., Tsai, P.A., Wessling, M., 2022a. Surface charge affecting fluid–fluid displacement at pore scale. Adv. Mater. Interfaces 9 (9), 2101895. https://doi.org/10.1002/admi.202101895
Kalde, A.M., Grosseheide, M., Brosch, S., Pape, S.V., Keller, R.G., Linkhorst, J., Wessling, M., 2022b. Micromodel of a gas diffusion electrode tracks in-operando pore-scale wetting phenomena. Small, e2204012. https://doi.org/10.1002/smll.202204012
Kintrup, J., Millaruelo, M., Trieu, V., Bulan, A., Mojica, E.S., et al., 2017. Gas diffusion electrodes for efficient manufacturing of chlorine and other chemicals. Electrochem. Soc. Interface 26 (2), 73–76. https://doi.org/10.1149/2.F07172if
Kunz, P., Hassanizadeh, S.M., Nieken, U., 2018. A two-phase SPH model for dynamic contact angles including fluidsolid interactions at the contact line. Transp. Porous Media 122 (2), 253–277. https://doi.org/10.1007/s11242-018-1002-9
Kunz, P., Hirschler, M., Huber, M., Nieken, U., et al., 2016a. Inflow/outflow with dirichlet boundary conditions for pressure in ISPH. J. Comput. Phys. 326, 171–187. https://doi.org/10.1016/j.jcp.2016.08.046
Kunz, P., Hopp-Hirschler, M., Nieken, U., 2019. Simulation of electrolyte imbibition in gas diffusion electrodes. Chem. Ing. Tech. 91 (6).
Kunz, P., Paulisch, M., Osenberg, M., Bischof, B., Manke, I., Nieken, U., et al., 2020. Prediction of electrolyte distribution in technical gas diffusion electrodes: from imaging to SPH simulations. Transp. Porous Media 132 (2), 381–403. https://doi.org/10.1007/s11242-020-01396-y
Kunz, P., Zarikos, I.M., Karadimitriou, N.K., Huber, M., Nieken, U., Hassanizadeh, S.M., et al., 2016b. Study of multi-phase flow in porous media: comparison of SPH simulations with micro-model experiments. Transp. Porous Media 114 (2), 581–600. https://doi.org/10.1007/s11242-015-0599-1
Lago, M., Araujo, M., 2001. Threshold pressure in capillaries with polygonal cross section. J. Colloid Interface Sci. 243 (1), 219–226. https://doi.org/10.1006/jcis.2001.7872
Lenormand, R., Touboul, E., Zarcone, C., 1988. Numerical models and experiments on immiscible displacements in porous media. J. Fluid. Mech. 189, 165–187. https://doi.org/10.1017/S0022112088000953
Li, W., 2020. Influence of Geometry and Wettability on Two-Phase flow in Porous Media. Dissertation. Universität des Saarlandes. https://doi.org//10.22028/D291-32767
Maier, L., Brosch, S., Gaehr, M., Linkhorst, J., Wessling, M., Nieken, U., et al., 2024. Convective drying of porous media: comparison of phase-field simulations with microfluidic experiments. Transp. Porous Media https://doi.org/10.1007/s11242-023-02051-y
Mayer, R.P., Stowe, R.A., 1965. Mercury porosimetry-breakthrough pressure for penetration between packed spheres. J. Colloid Sci. 20 (8), 893–911. https://doi.org/10.1016/0095-8522(65)90061-9
Mohammadi, M., Shafiei, M., Zarin, T., Kazemzadeh, Y., Parsaei, R., Riazi, M., 2024. Investigation of smoothed particle hydrodynamics (SPH) method for modeling of two-phase flow through porous medium: application for drainage and imbibition processes. Sci. Rep. 14 (1), 22144. https://doi.org/10.1038/s41598-024-73450-4
Monaghan, J.J., 1992. Smoothed particle hydrodynamics. Annu. Rev. Astron. Astrophys. 30 (1), 543–574. https://doi.org/10.1146/annurev.aa.30.090192.002551
Morris, J.P., 2000. Simulating surface tension with smoothed particle hydrodynamics. Int. J. Numer. Methods Fluids 33 (3), 333–353. https://doi.org/10.1002/1097-0363(20000615)33:3<333::AID-FLD11>3.0.CO;2-7
Morris, J.P., Fox, P.J., Zhu, Y., 1997. Modeling low reynolds number incompressible flows using SPH. J. Comput. Phys. 136 (1), 214–226. https://doi.org/10.1006/jcph.1997.5776
Mousavi, S.M., Sotoudeh, F., Chun, B., Lee, B.J., Karimi, N., Faroughi, S.A., 2024. The potential for anti-icing wing and aircraft applications of mixed-wettability surfaces – a comprehensive review. Cold. Reg. Sci. Technol. 217, 104042. https://doi.org/10.1016/j.coldregions.2023.104042
Moussallem, I., Jörissen, J., Kunz, U., Pinnow, S., Turek, T., et al., 2008. Chlor-alkali electrolysis with oxygen depolarized cathodes: history, present status and future prospects. J. Appl. Electrochem. 38 (9), 1177–1194. https://doi.org/10.1007/s10800-008-9556-9
Niblett, D., Niasar, V., Holmes, S., Mularczyk, A., Eller, J., Prosser, R., Mamlouk, M., 2023. Water cluster characteristics of fuel cell gas diffusion layers with artificial microporous layer crack dilation. J. Power Sources 555 (November 2022), 232383. https://doi.org/10.1016/j.jpowsour.2022.232383
Osiewacz, J., Löffelholz, M., Ellendorff, B., Turek, T., et al., 2024. Modeling mass transfer limitations driven by electrowetting in electrochemical CO2 reduction at silver gas diffusion electrodes. J. Power Sources 603, 234430. https://doi.org/10.1016/j.jpowsour.2024.234430
Patino-Narino, E.A., Idagawa, H.S., de Lara, D.S., Savu, R., Moshkalev, S.A., Ferreira, L.O.S., et al., 2019. Smoothed particle hydrodynamics simulation: a tool for accurate characterization of microfluidic devices. J. Eng. Math. 115 (1), 183–205. https://doi.org/10.1007/s10665-019-09998-2
Paulisch, M.C., Gebhard, M., Franzen, D., Hilger, A., Osenberg, M., Marathe, S., Rau, C., Ellendorff, B., Turek, T., Roth, C., Manke, I., 2021. Operando synchrotron imaging of electrolyte distribution in silver-based gas diffusion electrodes during oxygen reduction reaction in highly alkaline media. ACS Appl. Energy Mater. 4 (8), 7497–7503. https://doi.org/10.1021/acsaem.1c01524
Princen, H.M., 1969. Capillary phenomena in assemblies of parallel cylinders. II. capillary rise in systems with more than two cylinders. J. Colloid Interface Sci. 30 (3), 359–371. https://doi.org/10.1016/0021-9797(69)90403-2
Shadloo, M.S., Oger, G., Touzé, D.L., 2016. Smoothed particle hydrodynamics method for fluid flows, towards industrial applications: motivations, current state, and challenges. Comput. Fluids 136, 11–34.
Siper, 2024. *Siper*: Smoothed particle hydrodynamics in process engineering. https://www.icvt.uni-stuttgart.de/en/research/siper/. Online, accessed 8 October 2024.
Szewc, K., Pozorski, J., Minier, J.P., 2012. Analysis of the incompressibility constraint in the smoothed particle hydrodynamics method. Int. J. Numer. Methods Eng. 92 (4), 343–369. https://doi.org/10.1002/nme.4339
Tartakovsky, A.M., Meakin, P., 2005. Modeling of surface tension and contact angles with smoothed particle hydrodynamics. Phys. Rev. E Stat. Nonlinear Soft Matter Phys. 72 (2). https://doi.org/10.1103/PhysRevE.72.026301
Wendland, H., 1995. Piecewise polynomial, positive definite and compactly supported radial functions of minimal degree. Adv. Comput. Math. 4 (1), 389–396. https://doi.org/10.1007/BF02123482
Wenzel, R.N., 1936. Resistance of solid surfaces to wetting by water. Ind. Eng. Chem. 28 (8), 988–994. https://doi.org/10.1021/ie50320a024
Wiesner, F., Woodford, J., Sabharwal, M., Hesselmann, M., Jung, S., Wessling, M., Secanell, M., 2024. Unveiling the role of PTFE surface coverage on controlling gas diffusion layer water content. ACS Appl. Mater. Interfaces 16 (27), 34947–34961. https://doi.org/10.1021/acsami.4c04641
Wolff, H. J.M., Linkhorst, J., Göttlich, T., Savinsky, J., Krüger, A. J.D., Laporte, L., Wessling, M., 2019. Soft temperature-responsive microgels of complex shape in stop-flow lithography. Lab Chip . https://doi.org/10.1039/c9lc00749kPM-31802080
Woodward, J.T., Gwin, H., Schwartz, D.K., 2000. Contact angles on surfaces with mesoscopic chemical heterogeneity. Langmuir 16 (6), 2957–2961. https://doi.org/10.1021/la991068z
Xu, P., Agarwal, S., Albanese, J.F., Lefferts, L., 2020. Enhanced transport in gas-Liquid-Solid catalytic reaction by structured wetting properties: nitrite hydrogenation. Chem. Eng. Process. Process Intensif. 148, 107802. https://doi.org/10.1016/j.cep.2020.107802
Xu, R., Stansby, P., Laurence, D., 2009. Accuracy and stability in incompressible SPH (ISPH) based on the projection method and a new approach. J. Comput. Phys. 228 (18), 6703–6725. https://doi.org/10.1016/j.jcp.2009.05.032
Yadav, G.D., Dullien, F.A.L., Chatzis, I., Macdonald, I.F., 1987. Microscopic distribution of wetting and nonwetting phases in sandstones during immiscible displacements. SPE Reservoir Eng. 2 (02), 137–147. https://doi.org/10.2118/13212-PA
Zhang, C., Oostrom, M., Wietsma, T.W., Grate, J.W., Warner, M.G., et al., 2011. Influence of viscous and capillary forces on immiscible fluid displacement: pore-scale experimental study in a water-wet micromodel demonstrating viscous and capillary fingering. Energy Fuels 25 (8), 3493–3505. https://doi.org/10.1021/ef101732k
Zhao, B., MacMinn, C.W., Juanes, R., 2016. Wettability control on multiphase flow in patterned microfluidics. Proc. Natl. Acad. Sci. U.S.A. 113 (37), 10251–10256. https://doi.org/10.1073/pnas.1603387113
Zhao, X., Blunt, M.J., Yao, J., 2010. Pore-scale modeling: effects of wettability on waterflood oil recovery. J. Pet. Sci. Eng. 71 (3–4), 169–178. https://doi.org/10.1016/j.petrol.2010.01.011